

Can Robots “Taste” Grapes? Estimating SSC with Simple RGB Sensors

Thomas A. Ciarfuglia^a, Ionut M. Motoi^a, Leonardo Saraceni^a, Daniele Nardi^a

^aSapienza University of Rome Department of Computer, Control and Management Engineering, Rome, 00185, RM, Italy

Abstract

In table grape cultivation, harvesting depends on accurately assessing fruit quality. While some characteristics, like color, are visible, others, such as Soluble Solid Content (SSC), or sugar content measured in degrees Brix ($^{\circ}$ Brix), require specific tools. SSC is a key quality factor that correlates with ripeness, but lacks a direct causal relationship with color. Hyperspectral cameras can estimate SSC with high accuracy under controlled laboratory conditions, but their practicality in field environments is limited. This study investigates the potential of simple RGB sensors under uncontrolled lighting to estimate SSC and color, enabling cost-effective, robot-assisted harvesting. Over the 2021 and 2022 summer seasons, we collected grape images with corresponding SSC and color labels to evaluate algorithmic solutions for SSC estimation on embedded devices commonly used in robotics and smartphones. Our results demonstrate that SSC can be estimated from visual appearance with human-like performance. We propose computationally efficient histogram-based methods for resource-constrained robots and deep learning approaches for more complex applications.

Keywords: Precision Agriculture, SSC Estimation, Computer Vision, Robotics, RGB cameras

1. Introduction

The use of passive imaging sensors to measure agronomic properties of crops enables fast, non destructive monitoring that, when integrated with machinery or robots, can be efficiently scaled to cover entire fields. RGB cameras are commonly employed to monitor external conditions, such as detecting pests and diseases, while multi-spectral cameras are occasionally used to derive indices related to vegetation health. However, assessing internal crop properties presents a more complex challenge. Hyperspectral imagery (HSI) show potential in this area, as their ability to capture specific wavelength responses can be correlated with the absorption patterns of certain chemical properties. Nevertheless, hyperspectral cameras are typically slow to acquire images, highly sensitive to illumination conditions, and usually unsuitable for use on operational agricultural machinery.

These competing aspects collide with the desirable tension to bring more robots on the farming fields, in order to both face the shortage of workforce, but also to manage the crops in a more precise way. In fact, many cultivations are labor-intensive, and for various economic and social reasons, it is increasingly difficult to find human workers to perform operations such as harvesting. Table grape cultivation is an example of such labor-intensive cultivation that is increasingly popular in the markets but faces a workforce shortage. This shortage would be mitigated by the introduction of robot workers that could, to some extent, assist human workers in the field. To be able to do so, the robotic platform should be able to assess the quality and ripeness of the fruit using mainly passive sensors (active manipulation for perception would be orders of magnitude slower).



Figure 1: Computer Vision plays a crucial role in enabling automatic harvesting operations; however, the requirements for high-quality performance often conflict with the economic and practical constraints of robot design. This work demonstrates the development and deployment of a simple RGB-based algorithm for SSC and color quality estimation, addressing the complexities of field operations while utilizing cost-effective sensors.

While solutions to equip robots with hyperspectral cameras are becoming more prevalent, their high cost and operational complexity remain major barriers to widespread adoption. So, the question of designing a passive quality estimation system using low-cost, reliable, RGB cameras, or similar devices is still open.

This work addresses this question by validating its feasibility and proposing high-performance algorithmic solutions tailored for practical deployment in agricultural settings. In the following paragraphs, we provide a brief review of the relevant literature, highlighting key contributions to contextualize this study. For a broader overview of fruit ripeness estimation

*Corresponding author: ciarfuglia@diag.uniroma1.it

methods—particularly for grapes using hyperspectral and RGB imaging—we refer the reader to [11, 17].

1.0.1. Hyperspectral applications to agricultural robotics

Robots have been used for the monitoring and quality estimation of different crops and are now finding some industrial applications in high-value crops (wine grapes [20, 12], strawberries [23, 22], blueberries [19], among others). Some authors have explored specifically the quality estimation of fruits with hyperspectral sensors. In [6] an HSI device is mounted on an AGV to measure the TSS of Tempranillo wine grapes. The AGV moves along the vineyard row acquiring spectral data in a push-broom fashion. To achieve color constancy the authors perform an indirect calibration for exposure, while illuminant calibration was performed every 5m with a white reference. The impact of these choices on the accuracy of the estimation is not clear, and the authors report an RMS on °Brix estimate as low as 1.274. In addition, the method requires considerable post-processing time (5 hours), making it not well suited for robotic harvesting.

[18] propose a trailing cart mounting two HSI devices to monitor raspberries. However, the measurement is taken using an overarching arm from which a white reference is hung. [16] propose the Ladybug robot equipped with an HSI device built for low horticultural crops. The robot AGV is a straddle model, where the illumination constancy is granted through the use of a stroboscopic light.

In preparation for robotic use, [9] perform a very thorough experimentation using VIS-SWIR images to estimate SSC in four wine grapes varieties. The authors analyze the contribution of different wavelengths to the estimation algorithms in depth and apply various algorithms for the prediction. Across the proposed models (Partial Least Square, Random Forest, Convolutional Neural Networks, and Support Vector Machines) and four grape varieties they obtain an RMS error ranging from 1.70 to 2.20 °Brix.

In a follow-up study, to address the problem of illuminant estimation, [15] propose to learn the illuminant normalization through the use of an auto-encoder. The solution is similar to ours, in the sense that it learns the typical illuminant distribution, but loses the absolute metric accuracy of having a white reference in the scene. The authors explore four varieties of wine grapes, declaring RMSE values that range from 1.66 to 2.20 °Brix.

While the aforementioned approaches demonstrate the notable successes of HSI in agricultural robotics, they also exhibit several key limitations, including high sensor costs, operational complexity, lengthy post-processing times, and limited adaptability to crops where overarching machinery is impractical, such as table grapes. In contrast, the approach proposed in this work achieves comparable performance without relying on HSI, operates in real-time, and is thus better suited for integration into robotic systems.

1.0.2. RGB applications to fruit quality assessment

Given the limitations of HSI illuminant and color calibration and the cost of hyperspectral devices, many authors pro-

posed approaches based on standard RGB sensors. [1] have explored the use of color imaging combined with advanced numerical techniques, such as interval numbers (INs), and neural network regressors to estimate grape maturity indices (e.g., TSS, TA, and pH), demonstrating the feasibility of non-destructive and cost-effective methods for integration into autonomous harvesting systems. In this work, the authors declare a considerable 6.6259 MSE Baumé, which approximately corresponds to an RMSE of 4.63 °Brix.

[21] perform a very interesting analytical study on 180 samples of Kyoho grape berries using an RGB camera. The authors propose the use of some feature indexes, similar in principle to the well-known NDVI, but computed with the standard RGB channels, obtaining a very low cross-validation error of 0.78 °Brix (RMSE) on a dataset with a standard deviation of 1.37°. The study is performed in laboratory conditions, but it is nonetheless significant for our work, as it shows the effectiveness of data-driven estimations with simple RGB cameras.

[3] proposed a non-destructive estimation technique based on an RGB camera using random forest predictors trained on color histograms. The histogram was computed in CIELab color space by clustering the colors and then choosing the ones with the highest intrinsic variance. The classification task was performed on a 5-level quality scale, and no explicit SSC measurement was included in the labeling process. The experimental setup involved 200 bunches, evenly divided between Italia and Victoria varieties, shot with artificial illumination, and image features were computed after background subtraction.

This growing body of research on RGB-based estimation of internal crop characteristics highlights both the scientific and practical interest in this approach. However, to the best of our knowledge, existing methods either fall short of achieving the performance levels of HSI imaging or fail to transition effectively from controlled laboratory conditions to field environments with uncontrolled lighting.

Building on the challenges and opportunities highlighted in previous works, this study focuses on the problem of perception for quality estimation in table grape harvesting. Accurate quality estimation can enable robots to assist human workers or even surpass their capabilities during field operations. In high-quality table grape production, harvesting decisions typically follow a two-step process: an agronomist first samples grape bunches across the vineyard using a refractometer to measure SSC in °Brix. If the °Brix is sufficiently high, additional visual characteristics, such as color intensity and distribution, are evaluated. Workers are then instructed to harvest grape bunches based solely on appearance and location within the vineyard. While °Brix and color are not causally linked, they share latent ripening factors [8], allowing human experts to approximate °Brix from color to some extent. This work aims to replicate and enhance this human capability using data-driven methods and low-cost RGB sensors.

The contributions of our study are as follows:

- A dataset of table grape images collected across different seasons and with different sensors, labeled with both °Brix values and color categories following the afore-

mentioned agronomic procedure, thus enabling studies on SSC estimation in realistic field conditions.

- Experiments and user studies to explore the extent to which $^{\circ}\text{Brix}$ can be estimated from color alone. These insights informed the design of algorithms and highlighted key factors for future research.
- Two different estimation algorithms have been proposed and validated:
 - a) A lightweight method based on handcrafted features for constrained computational systems.
 - b) A deep, fully convolutional multi-task architecture that achieves high performance with limited training data.
- The methods do not require complex calibration and are designed for real-time use in robotic harvesting or mobile devices.

The paper is structured as follows: Section 2 describes the dataset that was collected and the estimation methods that were designed; Section 3 defines the experimental setup, and describes and comments on the experimental validation of the problem and the algorithms. Finally, Section 4 draws conclusions and outlines a path for future work.

2. Materials and Methods

2.1. Dataset

In this Section, we describe the data collection and labeling process.

2.1.1. Experimental Field

The experimental field is located in southern Lazio, Italy. The vineyard consists of two plots measuring approximately 114 m x 51 m (0.58 ha) and 122 m x 48 m (0.58 ha). The vineyards are structured as a traditional trellis system known as *Tendone*, with a wide distance between each plant (3 x 3 m). All structures are traditionally covered with plastic and netting to protect grapes from rain and hail. The plantations are all older than three years, healthy, and in full production, thus representing a typical working condition for the validation of agronomic activities such as fruit harvesting or vine pruning.

Among the varieties cultivated in this field, Black Pizzutello (*Pizzutello nero*), a distinct variety from the Lazio region, was selected due to its importance for the regional economy and color variability.

2.1.2. Data collection and labeling

We collected static images during two summer seasons using different camera sensors. Three different devices, across multiple years, have been used to collect the images. We employed a smartphone, a Reflex, and a Realsense d435i to represent some of the possible covariate shifts that occur between the collection of the initial data on the field by a farmer or an agronomist (smartphone), a high-quality sensor (reflex) and a

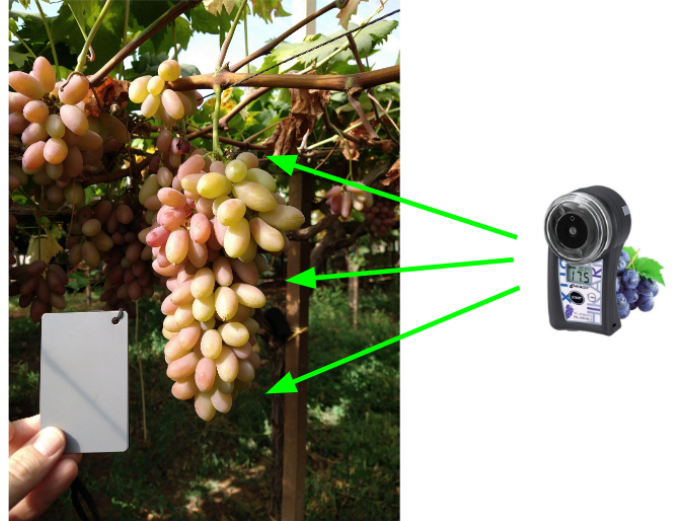


Figure 2: Example of an image collected with a gray card for white balance correction. An agronomist performs on-field measurements by randomly sampling the SSC of berries from the top, middle, and lower parts of the bunch and then averaging the values.

low-quality robotic camera (d435i). Table 1 depicts the working categories we used in this study. A more detailed description of all the data collected and the different characteristics is given in Appendix Appendix A for the interested reader.

Labels: All the images were labeled both for SSC and color. For SSC, we used an Atago Hikari PAL2 digital refractometer, capable of measuring berry sugar content (degree Brix, $^{\circ}\text{Brix}$) by contact without damaging the berry itself. This instrument has a range from 9° to 25° . Typically, depending on the grape variety, an SSC of 16° - 18° is considered good enough for harvesting. Since we are trying to assess how well the estimation based on appearance would perform compared to human performance, we adopted a labeling procedure similar to the SSC sampling performed by agronomists. Figure 2 visually illustrates the process. Every berry in a grape bunch has a different SSC, and the sugar concentration in each berry is also not uniform due to gravity. For this reason, common practice is to sample the SSC three times, from the top, middle, and bottom of the bunch, and then average the results. For consistency, the refractometer was placed on the side of the berry in each measurement. For color, a categorical classification was required. Based on agronomic production use cases, we defined a color quality chart with the help of experienced agronomists. The color scale goes from 1 to 6, with whole number increments, where 1 represents the best quality and 6 the worst. Usually, values of 1 and 2 are considered high-quality produce, while 3 is still acceptable for some markets. All the other values are considered unripe. This color index accounts for color saturation and distribution across the berries and the bunch. An example of the color variability is given in Fig: 3.

2.2. Estimation with Histogram Features

The main use-case for the estimators we design in this work is to be deployed on a robotic platform, embedded edge devices,

| Name | Split | # samples | SSC mean | SSC std | SSC MAD | Description |
|------------|-------|-----------|----------|---------|---------|--|
| $T1_{STD}$ | - | 112 | 17.19 | 2.43 | 1.99 | Phone images in JPG format captured in the 2021 season |
| $T1_{WB}$ | - | 112 | 17.19 | 2.43 | 1.99 | Phone images color corrected from RAW captured in the 2021 season |
| $T2_{STD}$ | tr | 212 | 16.23 | 2.52 | 2.02 | Phone images captured in JPG format during the 2021 season. |
| $T2_{STD}$ | te | 92 | 18.91 | 2.16 | 1.71 | Phone images captured in JPG format during the 2022 season. |
| $T2_{WB}$ | tr | 150 | 17.54 | 2.46 | 2.04 | Phone images captured in RAW format during the 2021 season. |
| $T2_{WB}$ | te | 92 | 18.91 | 2.16 | 1.71 | Phone images captured in RAW format during the 2022 season. |
| $T2_{ALL}$ | tr | 300 | 17.54 | 2.46 | 2.04 | Phone and reflex images in RAW format, 2021 season. |
| $T2_{ALL}$ | te | 92 | 18.91 | 2.16 | 1.71 | Phone and reflex images in RAW format, 2022 season. |
| $T3_{STD}$ | tr | 352 | 17.67 | 2.75 | 2.33 | All jpg images, across all seasons and devices. |
| $T3_{STD}$ | te | 44 | 15.96 | 1.68 | 1.36 | The test set contains images with SSC content close to the threshold (16° Brix). |
| $T3_{WB}$ | tr | 440 | 18.27 | 1.98 | 1.96 | All white balanced images, across all seasons and devices. |
| $T3_{WB}$ | te | 44 | 15.96 | 1.36 | 1.36 | The test set contains images with SSC content close to the threshold (16° Brix). |

Table 1: $T1_{STD}$ and $T1_{WB}$ consist respectively in jpg and raw versions of images collected with a smartphone camera during the 2021 season. $T2$ datasets are images collected with a smartphone camera, but where the training splits are from the 2021 season, and the test set from the 2022 season. In this case, there is no exact correspondence between $T2_{STD}$ and $T2_{WB}$ jpg and raw images. The $T3$ datasets serve a different purpose, as they combine images from the $T1$ and $T2$ datasets, mixing data across all seasons and devices, specifically the smartphone, Reflex (only for the WB variant) and d435i cameras. The $T3$ training set has more samples than the $T2$. At the same time, the $T3$ test set consists of images with SSC threshold quite close to the ripeness level for harvesting (16° for Pizzutello), making it significantly more challenging than the training set.

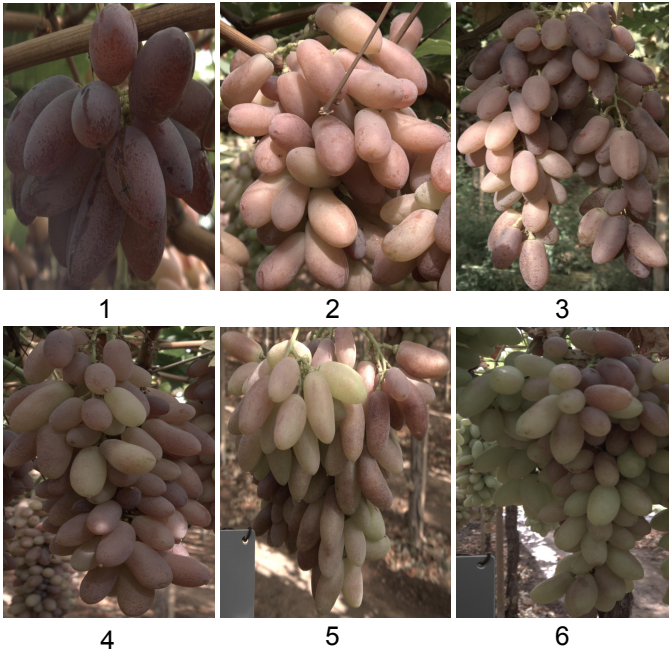


Figure 3: Examples of the six color levels for color classification. A clear distinction between categories may be challenging for an untrained eye. However, our labeling validation tests described in Section 3.1.2 indicate consistent labeling despite some uncertainty in the classification of neighboring classes.

or smartphone-like device, thus with limited memory and computational power. For this reason, the first approach is based on classic hand-crafted features, specifically on histograms. RGB channel histograms were chosen as the basic building blocks since the problem largely depends on color intensity and distribution. To capture distribution differences, we divided each bunch image into a grid of rectangular regions and computed the RGB histogram for each region. A key observation that can be made with this setup is that even with tight bounding boxes from the detector, some regions will often contain background information due to the shape of grape bunches. To address this issue, we modified the feature processing to retain only specific regions in a "cross-shaped" selection, as illustrated in Figure 4. This selection focuses on the areas of the image where grape content is most likely to be present.

To simplify hyper-parameter exploration, we defined three approaches for region selection: a "fat" cross-shaped pattern, a "thin" one, and one using all regions without any exclusion. More in detail, the three configurations are defined by the starting and ending cell in the column and row direction as follows:

$$\begin{aligned}
 \text{none} &: [0, n_{bin_x} - 1, 0, n_{bin_y} - 1] \\
 \text{fat} &: \left[\lfloor \frac{n_{bin_x}}{4} \rfloor, \lfloor \frac{3n_{bin_x}}{4} \rfloor, \lfloor \frac{n_{bin_y}}{4} \rfloor, \lfloor \frac{3n_{bin_y}}{4} \rfloor \right] \\
 \text{thin} &: \left[\lfloor \frac{n_{bin_x}}{4} \rfloor, \lfloor \frac{3n_{bin_x}}{4} \rfloor, \lfloor \frac{n_{bin_y}}{4} \rfloor, \lfloor \frac{n_{bin_y}}{2} \rfloor \right]
 \end{aligned} \tag{1}$$

We compared these approaches to determine the most effective feature selection strategy. In summary, the hyper-parameters that were considered while designing the features are:

- Image starting size (width, height)
- Number of cells in both the width and height directions
- The cross pattern used to remove the background



Figure 4: Each grape bunch in the scene is cropped based on the bounding box provided by the detector. The resulting image is then binned, with some bins dropped as they contain background information with high probability. This picture shows an example, but the actual bin size and dropping schemes are hyper-parameters described in Section 2. In this simple example, the n-uple defining `column` and `row` ranges described by Eq.1 would be [1,3,1,2]

- Use of HSV instead of RGB channels

We performed a hyper-parameter search for both the task of SSC and color degree estimation using Ridge Regression. For brevity, since color estimation is an easier task to perform, in Section 3 we omit the details of the experiments for color estimation, while the SSC ones are explored in depth.

2.3. Estimation with Multi-Task Learning DNN Architecture

As mentioned before, one of the research questions we are exploring is the correlation between the color of the berries and sugar content. The correlating latent factors are many and difficult to model explicitly. Among them are climate, weather, sunlight exposure, pruning strategies, and the use of nitrogen and other chemicals. Given this complex interaction between different factors, we decided to design a neural architecture that could extract common features to be used for both estimation tasks.

Our model is shown in Figure 5. To distill a feature vector, we employed an Auto-Encoder (AE) architecture, instead of using only a feature extraction backbone alone. The reason is that we are in a data-scarcity scenario, so having the additional reconstruction loss of the auto-encoder, focusing on appearance, helps in strengthening the back-propagation signal and reduces over-fitting. Our auto-encoder is a UNet with a ResNet18 backbone. In general, UNet-like architectures alone are not suitable for reconstruction problems, since the skip connections would cause the network to simply learn an identity function. Our architecture avoids this problem, by using the bottleneck feature output as the input for the feature extraction section. From those features, a convolutional block is used to extract the features that are then fed to the task-specific heads. The two heads have the same structure, but in the case of color estimation, the outputs are logits for the multi-class problem, while for the SSC estimation are the actual estimations.

The loss for the architecture is the combination of the reconstruction loss of the AE (pixel-wise Mean Squared Error (MSE)), with the addition of a Mean Absolute Error (MAE) loss for the SSC estimate, and a Cross-Entropy loss for the color classes:

$$\mathcal{L}_{MT} = \mathcal{L}_{rec} + \alpha \mathcal{L}_{color} + \beta \mathcal{L}_{brix} \quad (2)$$

where α and β are weighting factors to balance the different contributions of the three losses, whose values have been cross-validated together with other hyper-parameters.

2.3.1. Hyper-parameter Validation

Hyperparameter selection in multi-task learning requires identifying a single metric \mathcal{S} that effectively summarizes performance across different models, which is particularly challenging when tasks differ significantly.

For SSC estimation, mean absolute error (MAE) on the °Brix scale provides an intuitive measure. Color estimation, however, is better assessed using Balanced Accuracy (A_{color}) due to the categorical nature of the target variable (although the cross-entropy loss is also applicable it is less interpretable). We combine these two metrics to evaluate the overall performance of the estimators. However, since the metrics are in different scales and units we normalize them using a factor η .

Our evaluation criteria also align with agronomic quality standards, emphasizing the importance of avoiding the harvest of unripe bunches, while allowing for some variation in quality among ripe bunches. This is achieved by introducing hinge-like penalties that apply only when estimations fall below predefined quality thresholds for SSC (t_{brix}) and color (t_{color}) estimation, ensuring that models are primarily evaluated on their ability to meet minimum quality standards. The final score, \mathcal{S} integrates the normalized performance metrics and the agronomic quality criteria.

The formal definition of the score \mathcal{S} is the following:

$$\mathcal{S} = \eta(1 - A_{color}) + \mathcal{L}_{brix} + \mathcal{L}_{CH} + \mathcal{L}_{BH} \quad (3)$$

$$\mathcal{L}_{BH} = \max(0, \mathcal{L}_{brix} - t_{brix})^\rho \quad (4)$$

$$\mathcal{L}_{CH} = \max(0, -\eta(A_{color} - t_{color}))^\rho \quad (5)$$

where ρ is the degree of the two hinge penalties \mathcal{L}_{BH} (for °Brix) and \mathcal{L}_{CH} (for color), set to 2 in all our experiments. t_{brix} and t_{color} represent the agronomic quality thresholds for °Brix and color, respectively, and η is the normalization factor between SSC and color scores. In our experiments, $t_{brix} = 2.5$ °Brix, which is comparable with the standard deviation of the training data, and $t_{color} = 0.8$, since an error rate of 80% is usually considered acceptable for human performance in this context [14]. The normalization factor is empirically set as

$$\eta = \frac{t_{brix}}{t_{color}}. \quad (6)$$

3. Experiments

In designing the experimental setup, we had two main aims. The first one was to give an initial answer on factors are rele-

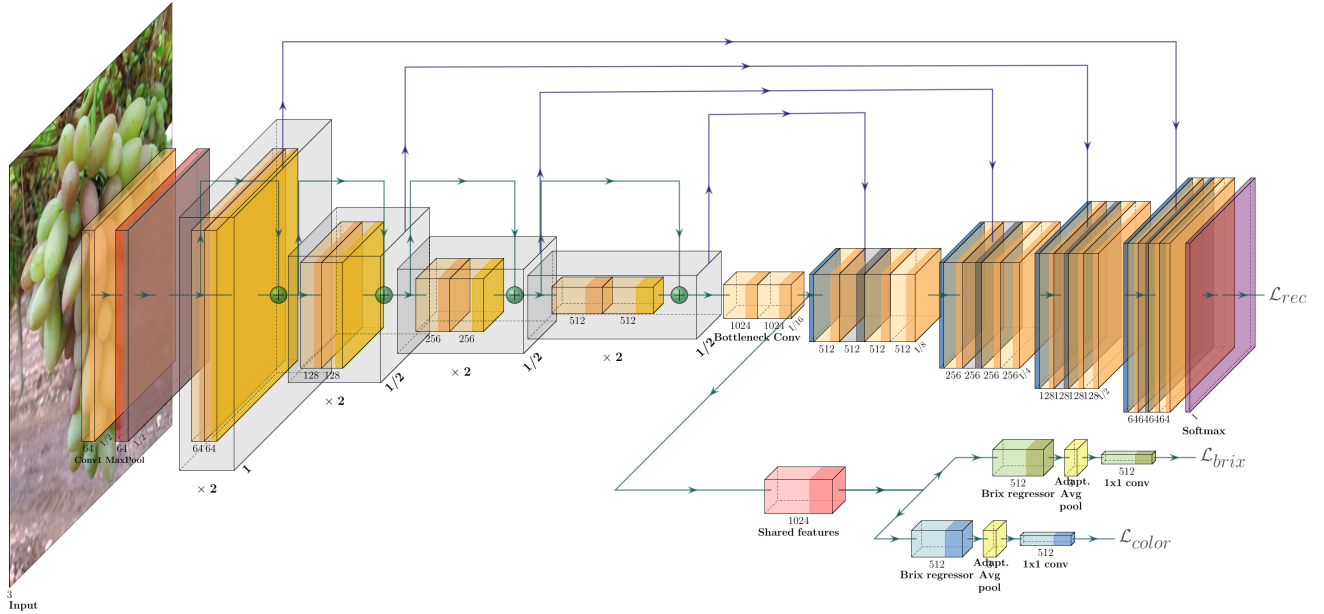


Figure 5: The multi-task network is based on a U-Net [13] with a *ResNet18* [7] backbone, designed to encode the image into a compact representation. Features extracted from the bottleneck layer are fed into a two-head estimator: one for SSC (regression) and another for color (classification). The two heads share a common “neck,” a CNN with 512 output channels, ensuring part of the representation is shared between the tasks. Each head has a symmetrical structure, comprising three CNN blocks that progressively reduce the feature size, followed by adaptive average pooling [24] and a 1x1 convolution [10] for the final estimation.

vant in estimating SSC from appearance, in order to better understand the problem for future work and data collection campaigns. The second aim is to validate the proposed features and estimator models. This section begins with the validation of the collected dataset, followed by a description of the exploratory experiments. Finally, we describe the validation of our proposed features and models, together with the ablation studies. The data and code for all the experiments can be found on the accompanying GitHub repository¹.

3.1. Exploratory User Studies

3.1.1. Human Evaluated SSC and Color Correlation

In order to have an initial human performance baseline and to assess the experts’ actual capacity to estimate ripeness from appearance, we performed a specific test. We gave to a number of agronomists with experience in table grape ripeness estimation, 100 grape images, for which a °Brix ground truth was collected with the technique described in Fig. 2. We used the JPG smartphone images collected during the first data collection session (24 September 2021) for Pizzutello Nero. The images were given without any other hint to the experts, asking them to express a numeric evaluation, on a scale from 1 to 10, of the degree of color, peduncle lignification stage, and berry shape. Note that this color scale is not the same as the one defined in Section 2.1.2. The reason is that this experiment uses a human-friendly decimal scale, while the one defined previously is to be used by a classification algorithm. In addition to

the aforementioned parameters, the agronomists were asked to guess if the °Brix for the sample was high enough for harvesting purposes (in this case, ≥ 17). Table 2 summarizes the experiment variables name and meaning. First, we checked the correlation between human-given values of c_val , l_val and r_val and the measured mean °Brix value, m_brix to explore the hypothesis where color and other visual elements could be a good predictor for sugar content.

In Fig. 6 the correlation matrix is shown. The correlation score between the average °Brix (m_brix) and color evaluation (c_val) is 0.505, with $p < 0.001$ and $CI = [0.342, 0.638]$, the correlation between m_brix and lignification (l_val) is 0.337, $p < 0.001$ and $CI = [0.151, 0.501]$, while the correlation with berry shape (r_val) score is much lower, -0.038 way below any significance threshold.

The observed correlation between human expert visual assessment and measured °Brix values suggests that a data-driven algorithm could achieve human-level accuracy in estimating grape quality for harvesting decisions. Even if there is a significant correlation with the lignification of the peduncle, in this work we focused on the color, leaving the use of peduncle lignification as a predictor for future work.

The second outcome of this experiment was to define some human harvesting performance baselines. For this question, we consider the c_class , the color category given by the agronomists to each sample, as the harvesting prediction and the thresholded values b_class as the binary labels. The precision and recall values are respectively 0.43 and 0.83, which means a false discovery rate (type I error rate) of 0.56 and false negative rate (type

¹To be disclosed upon publication

| Feature | description |
|--------------|---|
| v1, v2, v3 | Upper, middle and lower °Brix measurements. |
| m_brix | Mean °Brix computed from v1, v2, v3. |
| m_b_t | Rounded m_brix (unused). |
| b_class | Binary °Brix class for harvesting (Sufficient, Insufficient). Computed from m_brix with threshold 17°. |
| c_val | Expert given score for color development after <i>varaison</i> , on a scale from 1 to 10. |
| c_class | Binary color class for harvesting (Sufficient, Insufficient). Computed from c_val with threshold 6. |
| l_val, r_val | Expert given scores for lignification and berry shape development, respectively, on a scale from 1 to 10. |

Table 2: These are the parameters considered by the agronomist in the exploratory experiment to assess the correlation between °Brix and human color evaluation.

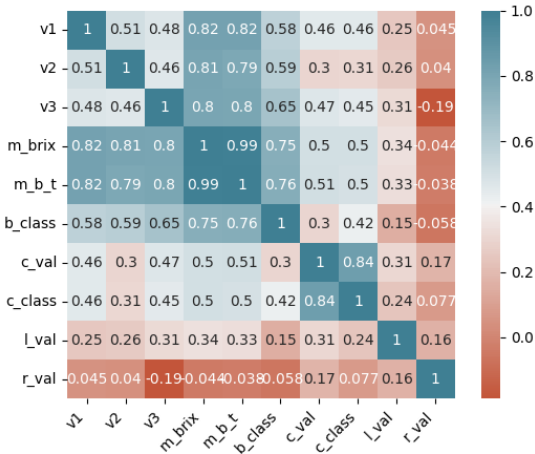


Figure 6: Correlation matrix of the parameters estimated by human experts looking to a sample of 50 images of table grape bunches, as described in Section 3.1. The key factor for our evaluation is the correlation between the SSC guess (m_brix) and the evaluation of bunch color (c_val).

II error rate) of 0.17.

It is important to state that in the case of harvesting, type I errors (false positives) have a higher cost than type II since all the ripe bunches left on the vine tree will be eventually harvested, while the harvested unripe bunches have to be disposed of. We see that by simply collecting the table grape bunches with a color class over the threshold of 6 (the definition for the c_class attribute) a lot of unripe bunches are collected due to °Brix to color mismatch. One question that arises then is if by increasing the threshold for c_class , it would be possible to trade type I errors for type II errors. Computing the precision and recall scores for a c_class value obtained with a threshold of 7 for example, we get respectively 0.35 precision and 0.37 recall, which is an increase in both error types. This test shows that, while °Brix and color are correlated on the broad range of the color scale of this experiment, at the same time, the relationship is not quite linear, i.e. there are both a considerable number of insufficiently colored bunches that have sufficient °Brix, and highly colored bunches with insufficient °Brix. The high number of bunches on a borderline situation that the experts misclassify shows that the question of training an appearance-based estimator is a non-trivial one.



Figure 7: Some examples of pictures of the same table grape bunches were presented to agronomists on different occasions to test whether human experts consistently evaluated bunch ripeness, regardless of color correction, as described in Section 3.1.2

3.1.2. Color Constancy effect on Human Evaluation of Color

One of the early questions that arose from data collection was to what extent the camera image processing pipeline could influence the possibility of estimating the correct color stage, and therefore influence the °Brix estimate. Smartphone cameras, like most camera devices, do not process the raw signal from their CCD/CMOS sensors for radiation accuracy, but more for aesthetic purposes. This means that color accuracy is often lost in the nonlinear pipeline that transforms raw images into JPGs. A second consideration was related to the difference between the human vision system and a camera device. We know that human experts and workers alike are able to guess ripeness from appearance, but to what extent some of the peculiarities of the human vision system influence this guess (e.g. consider the brightness constancy effect) is unknown. While color perception is a complex topic, we focused our analysis on a specific question: whether human experts assign significantly different color labels when viewing white-balanced versus standard images. We selected 50 images from a single field trip that had paired raw and JPG image formats. The raw image was processed only with debayering and white balancing using the grey card. (Figure 7 shows some examples).

We presented all 100 images in random sequence to a group of agronomist experts, without revealing that each bunch appeared twice. The experts labeled the color quality of each image using the color scale described in Section 3, without performing any other manipulation or consideration. The null hypothesis is that there is no difference in labeling standard and white-balanced images apart from some generic labeling noise. If we define the mean group labeling error as:

$$\mu_i = \mathbf{E} \left[L_{GT_i} - L_{exp_i} \right] \quad (7)$$

where $i \in [0, 1]$ is the sample group, L_{GT_i} is the hypothetical ground truth color label for a random sample from group i , and L_{exp_i} is the label that an expert gives for the same random sample. Furthermore, we denote with Y_i the sample mean of the difference between the true label and the estimated one. Then, we can state that $Y_1 - Y_0$ is an unbiased normally distributed estimator of $\mu_1 - \mu_0$, and thus we can formulate the following null hypothesis:

$$\mathcal{H}_0 : \mu_1 - \mu_0 = 0 \quad (8)$$

which we can easily test for significance with a z-test.

Analysis of the results revealed only a small difference between expert labels for the two groups, with a mean difference of 0.1 and a standard deviation of 0.50. The paired test for the sample batch gives a z-statistic of 1.4 ($p=0.17$), which does not provide sufficient evidence to reject \mathcal{H}_0 . While a larger sample size might yield more definitive results, we chose instead to focus on the estimation algorithms, which are the main subject of our study. In particular, we included the comparison between white-balanced images and standard images into the cross-validation of the histogram-based features to gain deeper insights.

3.2. Histogram based color and °Brix estimation

This Section first outlines the experimental setup used to evaluate histogram features and subsequently presents the results.

3.2.1. Description

Given the exploratory experiments described in the previous Sections 3.1.1 and 3.1.2, we designed the histogram features as described in Section 2.2 and use them to train regression and classification models to predict SSC and color level, respectively.

The following experiments were conducted for both color estimators (multi-class classification) and SSC estimators (°Brix regression). Given the higher difficulty of SSC estimation compared to exterior color evaluation, the following description focuses on SSC estimation, while the tables and figures summarize the results for both SSC and color estimation.

The main question addressed in these experiments is the overall performance of the histogram-based algorithms and the influence of hyper-parameters. A number of grid hyper-parameter searches using Ridge Regression were conducted on a limited dataset, specifically the $T1_{STD}$ and $T1_{WB}$ splits, to mitigate distribution shifts due to different camera sensors and seasons during the initial analysis. These splits contain 112 samples each, divided into 89 train images and 23 validation images. The training images were augmented with horizontal flips, resulting in a total of 178 training images. As previously mentioned, both standard JPG and white-balanced images were evaluated to assess the influence of post-processing on the feature-based algorithms.

To set a baseline for this approach, we considered the intrinsic variability training and test data. The $T1$ datasets have a mean of 17.19 °Brix, a standard deviation of 2.43 °Brix, and a

mean absolute deviation (MAD) of 1.99 °Brix. Appendix Appendix A provides more details on the statistical properties of the datasets. The naive predictor, which always predicts the mean °Brix values of the training set, resulting in a mean absolute error (MAE) equal to the MAD, serves as the lower bound for estimator performance.

3.2.2. Discussion

A grid search on the aforementioned hyper-parameter ranges, requiring training 3888 different models, was performed using the Weights & Biases experiment tracking framework [2] to compare and analyze the results. Further details of the hyper-parameter search are provided in Appendix Appendix B, while this section focuses on the key findings. The correlation coefficient of each feature with the validation error has been computed and is shown in Fig. 8a. In addition, Table 3 shows the 10 best runs for the *low_res* images.

As expected, given the limited number of samples in the $T1$ datasets, the regularization parameters and those influencing feature vector length had the greatest impact on the final results. Furthermore, image resolution proved irrelevant, suggesting the safe use of lower-resolution images for computational efficiency in embedded applications. This is consistent with the feature construction process, where binning and averaging naturally remove the complexities of high-level details. Finally, and most notably, both Fig.8a and Table 3, indicate that using an alternative color space, such as HSV, helps in finding better coefficients for the Ridge Regression.

Focusing solely on the 1296 lower-resolution runs, the best-performing models have validation MAE of 1.45, with different combinations of hyper-parameters that have in common a low feature count relative to the regularization value. Table 3 summarizes some of these top-performing runs, all exhibiting MAE lower than the baseline $brix_{mad}$ of 1.99. The best run reaches a **27%** improvement over the baseline, a notable result considering the limited training data. Figure 8b displays the validation errors for different α values (on a logarithmic scale), for both color-corrected and standard images. The most interesting feature of the plot, which is a common trend in all similarly produced plots, is the consistently inferior performance of the models trained on color-corrected images compared to their standard counterparts with identical hyper-parameters.

3.3. Multi-task Learning DNN

The SSC and color distribution can be viewed as conditioned on the environmental and agronomic parameters of the field we are considering. While both the color and the SSC depend on the internal chemical state of the berries, this state itself is influenced by environmental factors such as growing conditions, training practices, and nutrient availability. The overall appearance of the grape bunches is also affected by these factors, which we assume are homogeneous across the vineyard.

The architecture of the multi-task network, illustrated in Fig. 5, reflects this reasoning. The encoder component captures common features in appearance variations that may correlate with the internal chemical state of the grapes. These shared

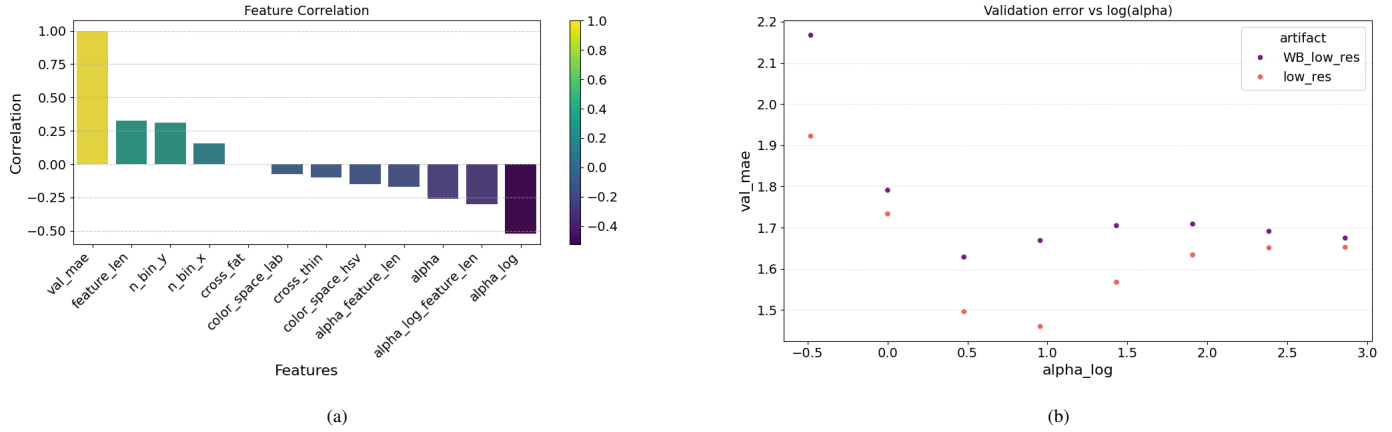


Figure 8: a) Correlation between validation error and hyper-parameters for the top 10% performing runs. This plot highlights the direction (positive or negative) of the correlation. b) Test error for models with hyper-parameters identical to the best model shown in Table 3, but with varying α values and color correction. The consistent lower error for models trained on standard images compared to color-corrected images gives a clear answer to the question raised in Section 3.1.2.

| Test MAE | Val MAE | Train MAE | α | n_{bin_x} | n_{bin_y} | $cross$ | $color_space$ | $feature_len$ | $\log(\alpha) \times feature_length$ |
|----------|----------|-----------|----------|-------------|-------------|---------|----------------|----------------|---------------------------------------|
| 1.459898 | 2.098344 | 1.583124 | 9.000000 | 16 | 8 | none | hsv | 128 | 122.143041 |
| 1.509351 | 2.129067 | 1.548176 | 9.000000 | 8 | 16 | none | hsv | 128 | 122.143041 |
| 1.522208 | 2.141015 | 1.614265 | 3.000000 | 8 | 8 | none | hsv | 64 | 30.535760 |
| 1.509816 | 2.144949 | 1.178387 | 9.000000 | 8 | 32 | none | hsv | 256 | 244.286082 |
| 1.507421 | 2.164503 | 1.619756 | 1.000000 | 16 | 8 | thin | lab | 80 | 0.000000 |
| 1.495739 | 2.164640 | 1.254232 | 3.000000 | 16 | 8 | none | hsv | 128 | 61.071521 |
| 1.517718 | 2.181812 | 1.431866 | 3.000000 | 16 | 8 | fat | hsv | 96 | 45.803640 |
| 1.523156 | 2.193494 | 1.719893 | 0.330000 | 8 | 8 | thin | lab | 40 | -19.259442 |
| 1.431197 | 2.200048 | 1.189874 | 3.000000 | 8 | 16 | none | hsv | 128 | 61.071521 |
| 1.491955 | 2.327332 | 1.225366 | 1.000000 | 16 | 8 | thin | hsv | 80 | 0.000000 |

Table 3: The top 10 histogram-based models, ranked by validation mean absolute error (Val MAE), along with their corresponding hyper-parameters values. Some trends discussed in Section 3.2, such as the importance of alternative color spaces like HSV, are clearly evident.

features are then leveraged by two separate prediction heads to estimate the color class and SSC in parallel. As before, in the following we first give a description of the experiment and then discuss the results.

3.3.1. Description

The $T2$ dataset (Table 1) is used to evaluate the covariate shift due to the variability in treatments between consecutive seasons while keeping the sensor type fixed. Since phone images were captured in both raw and JPG formats, the $T2$ splits include standard ($T2_{STD}$) and white-balanced ($T2_{WB}$) versions. This allows for a direct comparison of performances between standard JPG and color-corrected images, under identical hyper-parameters and for the same grape bunch instances. In both cases, data from the 2021 season serves as the training and validation sets, while the data from the 2022 season are used as the test set. The $T2_{ALL}$ split consists only of color-corrected images since it includes reflex camera images that have been captured in raw format and subsequently color-corrected using the gray card. This split helps assess to some degree the effect of using two different camera devices to capture the same instances with the same perspective. The $T3$ splits combine images from all devices across both seasons, including both color-corrected and standard versions.

Appendix Appendix C and Table C.10 summarize the hyper-parameter ranges considered for the experimental evaluation. We performed 4912 runs on a DGX server with four A100 GPUs. Each run was trained for 200 epochs with hyper-band early stopping. For all the experiments we used a *ResNet18* backbone [7], exploring both the effect of pretraining on *ImageNet* [4] and training from scratch. Hyper-parameter relevance was assessed using the BCH metric described in Section 2.3.1. While the complete details on the analysis of the importance of each hyper-parameter are described in Appendix Appendix C, in the following Section we discuss the most relevant findings.

3.3.2. Discussion

We begin our analysis with the 1002 runs performed on the $T2$ splits. Since we sampled a wide range of models via random search, we concentrate on the best 25% of the total runs to discuss the influence of hyper-parameters. Figure 9a presents the correlation between the hyper-parameters and the BCH metric, while Table 4 lists the top 10 performing runs. The multi-task network effectively learns good models for both SSC and color estimation. Apart from the typical learning parameters, the ones that show more influence on the performance results are image size (particularly width) and color space (rarely RGB among top performers). However, no single hyper-parameter shows high correlation values, indicating a complex relationship linking the parameters to the error. Another consideration is that α is typically ten times larger than β , giving a rough estimate of the relative weight of the corresponding losses for the final results. Moreover, the benefit of the additional augmentations appears less substantial than initially anticipated. It is important to note that the lowest MAE for SSC and the highest accuracy for color estimation are not achieved at the same epoch. This is unsurprising, as perfectly correlated feature learning for

distinct tasks is unlikely, even with strong underlying correlations. Therefore, when using a single feature extractor, a trade-off must be made between optimizing for SSC or color estimation. If computational resources permit, employing two different feature extractors (i.e., different checkpoints) allows for independent optimization and potentially better performance on both tasks.

Similar trends emerge from the experiments on the $T3$ splits. Figure 9b shows the correlations of the hyper-parameters with the error, and Table C.13 displays the best-performing runs. Again, the α to β ratio is confirmed, along with the general preference for having higher image width values. The $T3$ test set, captured with a Realsense d435i, introduces a covariate shift due to its lower resolution and different white balance settings compared to the phone and reflex cameras used for training. This difference might explain the increased relevance of blur-related parameters in the augmentation.

Following the analysis conducted for histogram features in Section 3.2, we compare the best $T3$ run with runs using the same hyper-parameters but trained on white-balanced images. Unlike the histogram feature case with a single regularization parameter, the multi-task model utilizes two (α and β). Given what was observed from the experiments, that the ratio of the α and β values is more important than their absolute value, we use this as a parameter to compare the impact of using color-corrected images versus using the standard JPG ones. Similarly to the analysis presented in Section 3.2, we select the 150 best-performing runs and the ones with matching hyper-parameters (except for $\log(\alpha/\beta)$) and use them to extract a general trend shown in the scatter plot in Figure 10. The regression lines for both standard and white-balanced image sets exhibit nearly identical slopes (-0.212 and -0.216 , respectively), and the difference between the lines is small, with largely overlapping confidence intervals. This suggests that the multi-task model effectively extracts relevant features regardless of color correction, with performance oscillations likely stemming from training data variability and other hyper-parameters.

To conclude, the best-performing runs for SSC estimation achieve MAE values as low as 1.55 (1.57) for the model trained on the $T2_{STD}$ ($T2_{WB}$) split, and 1.11 (1.10) for the one trained on the $T3_{STD}$ ($T3_{WB}$) split. Considering that the MAD values for the $T2$ and $T3$ test splits are 1.71 and 1.36, respectively, the performance gain of the multi-task models is 9.3% (8.1%) for the $T2$ case and 18.4% (19.1%) for $T3$ case. These results confirm the negligible impact of color correction on the multi-task model performance, as observed in the regression analysis. The superior performance of the white-balanced model on the $T3$ dataset can be attributed to the automatic white balancing performed by the d435i camera used for collecting the $T3$ test set.

4. Conclusions

This work addressed the problem of estimating soluble solid content (SSC) in grapes using RGB data acquired in the field. While numerous studies explore laboratory equipment and hyperspectral data for SSC estimation through visual sensors, this

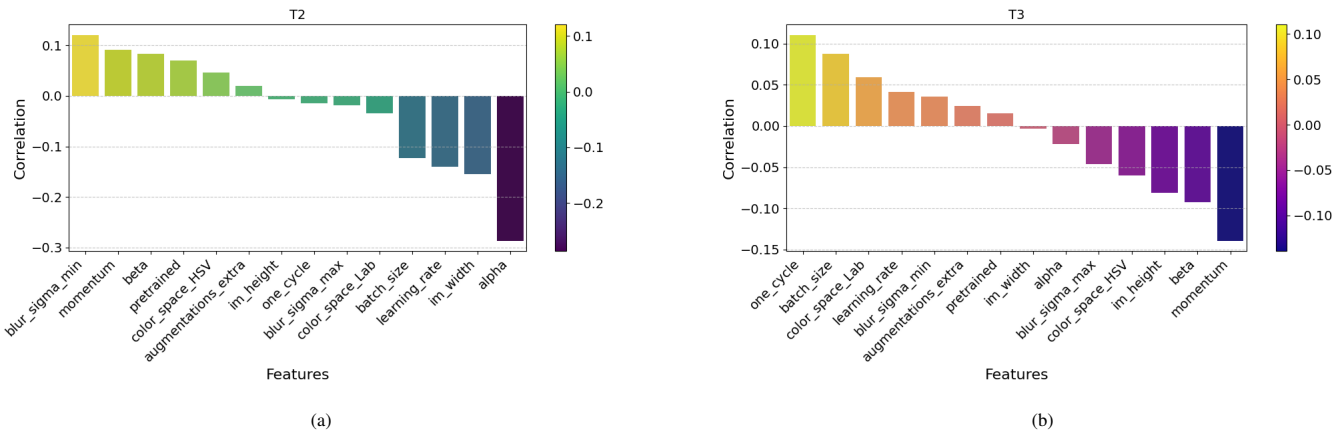


Figure 9: *Multi-task network hyper-parameter correlation* - These histograms show the correlation between the validation error and the hyper-parameters computed on the 25% best performing runs. a) *T2* dataset: it can be noted that the main influence comes from the classical parameters that impact any DNN training (learning rate, batch size, regularization parameters), though image size and color space remain relevant. More insights on this can be extracted from Table 4. b) *T3* dataset: similar trends are observed as in (a), with classical DNN training parameters having the most significant impact. The increased importance of blur parameters suggests the potential benefits of data augmentation strategies in mitigating the effects of covariate shifts due to variations in camera devices.

| Val BCH | Val SSC MAE | Val Acc | α | β | im_width | im_height | momentum | learning_rate | batch_size | blur_ σ _min | blur_ σ _max | pretrained | one_cycle | HSV | Lab | augment_extra |
|----------|-------------|----------|----------|---------|-------------|--------------|----------|---------------|------------|---------------------|---------------------|------------|-----------|-------|-------|---------------|
| 4.076824 | 1.555511 | 0.673913 | 500 | 50 | 256 | 256 | 0.990000 | 0.000001 | 64 | 0.100000 | 2 | False | False | False | True | True |
| 4.188802 | 1.832541 | 0.663043 | 1000 | 1000 | 256 | 64 | 0.950000 | 0.000001 | 32 | 0.500000 | 4 | False | True | False | True | False |
| 4.265176 | 1.653810 | 0.554348 | 100 | 10 | 64 | 256 | 0.950000 | 0.000050 | 64 | 0.500000 | 2 | True | False | True | False | False |
| 4.312880 | 1.732056 | 0.619565 | 500 | 100 | 256 | 64 | 0.800000 | 0.000050 | 128 | 0.100000 | 2 | True | True | True | False | True |
| 4.346299 | 1.579317 | 0.630435 | 1000 | 100 | 256 | 128 | 0.800000 | 0.000050 | 128 | 0.010000 | 4 | False | True | True | False | False |
| 4.412035 | 2.160111 | 0.532609 | 500 | 100 | 64 | 128 | 0.990000 | 0.000050 | 128 | 0.010000 | 2 | False | True | True | False | False |
| 4.453714 | 1.795929 | 0.684783 | 1000 | 500 | 256 | 256 | 0.950000 | 0.000010 | 128 | 0.010000 | 2 | False | False | False | True | True |
| 4.496901 | 1.891276 | 0.673913 | 100 | 50 | 256 | 128 | 0.900000 | 0.000050 | 128 | 0.500000 | 2 | True | True | True | False | True |
| 4.536293 | 1.629490 | 0.521739 | 100 | 100 | 256 | 128 | 0.900000 | 0.000050 | 64 | 0.500000 | 2 | False | False | False | False | False |
| 4.598450 | 1.620318 | 0.695652 | 10 | 1 | 256 | 256 | 0.990000 | 0.000050 | 128 | 0.100000 | 4 | False | True | False | True | True |

Table 4: The best ten runs on *T2* split.

study is among the few to focus exclusively on the practical scenario of RGB data collected directly in field conditions. The complexity of this task arises from covariate shifts inherent to the problem, including seasonal variations and differences in imaging devices.

To tackle this challenge, a dataset spanning multiple years was collected, incorporating data from various camera devices and annotated for SSC and color quality based on agronomic practices. Human performance in assessing the correlation between color and SSC was evaluated through two user studies, which informed the design of data-driven algorithms for estimating both SSC and color.

Two algorithmic approaches were explored: a light-weight method using classical handcrafted features, suitable for devices with limited computational power, and a multi-task neural network architecture that, while more computationally demanding, effectively leverages correlations between visual appearance (color and shades) and SSC. Both methods were experimentally validated using field-collected data from the Pizutello Nero grape variety. Results indicate that the proposed techniques achieve reliable SSC estimation with a reasonable margin compared to the average human estimator. Furthermore, experiments demonstrated some robustness to covariate shifts, including seasonal variations and device differences, positioning the proposed solutions as viable prototypes for low-cost, on-field applications where frequent data collection and labeling are challenging.

We release all the data, code, trained models, and training scripts used in this study. Future work will focus on refining and aligning these low-cost estimators and benchmarking them against hyperspectral approaches.

Acknowledgments

 This work is part of a project that has received funding from the European Union’s Horizon 2020 research and innovation programme under grant agreement No. 101016906 – Project CANOPIES

 This work has been partially supported by project AGRITECH Spoke 9 - Codice progetto MUR: AGRITECH ”National Research Centre for Agricultural Technologies” - CUP CN00000022, of the National Recovery and Resilience Plan (PNRR) financed by the European Union ”Next Generation EU”.

This work has been partially supported by Sapienza University of Rome as part of the work for project *H&M: Hyperspectral and Multispectral Fruit Sugar Content Estimation for Robot Harvesting Operations in Difficult Environments*, Del. SA n.36/2022.

References

- [1] Bazinas, C., Vrochidou, E., Kalampokas, T., Karampatea, A., and Kaburlasos, V. G. (2022). A non-destructive method for grape ripeness estimation using intervals’ numbers (ins) techniques. *Agronomy*, 12(7).

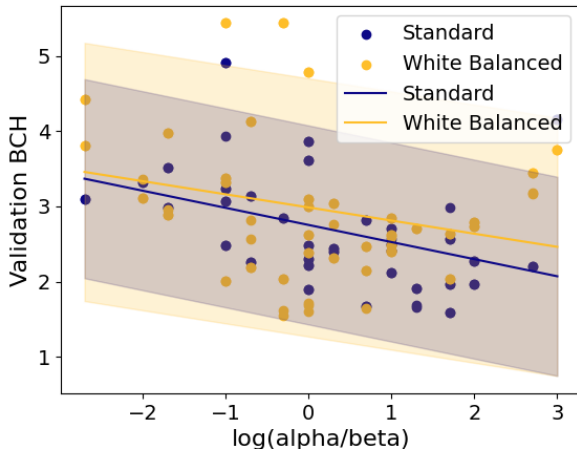


Figure 10: Linear regression analysis of runs with hyper-parameters similar to the top 10 runs on the $T3_{STD}$ and $T3_{WB}$ datasets. The shaded area represents the 95% confidence interval. While the models trained on color-corrected samples present slightly higher values on average, the smaller difference compared to Fig. 8b suggests no practical advantage in using standard images over the white-balanced ones in this context.

[2] Biewald, L. (2020). Experiment tracking with weights and biases. Software available from wandb.com.

[3] Cavallo, D. P., Cefola, M., Pace, B., Logrieco, A. F., and Attolico, G. (2019). Non-destructive and contactless quality evaluation of table grapes by a computer vision system. *Computers and Electronics in Agriculture*, 156:558–564.

[4] Deng, J., Dong, W., Socher, R., Li, L.-J., Li, K., and Fei-Fei, L. (2009). Imagenet: A large-scale hierarchical image database. In *2009 IEEE Conference on Computer Vision and Pattern Recognition*, pages 248–255.

[5] Grömping, U. (2009). Variable importance assessment in regression: linear regression versus random forest. *The American Statistician*, 63(4):308–319.

[6] Gutiérrez, S., Tardaguila, J., Fernández-Novales, J., and Diago, M. (2019). On-the-go hyperspectral imaging for the in-field estimation of grape berry soluble solids and anthocyanin concentration. *Australian Journal of Grape and Wine Research*, 25(1):127–133.

[7] He, K., Zhang, X., Ren, S., and Sun, J. (2016). Deep residual learning for image recognition. In *2016 IEEE Conference on Computer Vision and Pattern Recognition (CVPR)*, pages 770–778.

[8] Jackson, D. I. (1986). Factors affecting soluble solids, acid, ph, and color in grapes. *American Journal of Enology and Viticulture*, 37(3):179–183.

[9] Kalopesa, E., Karyotis, K., Tziolas, N., Tsakiridis, N., Samarinas, N., and Zalidis, G. (2023). Estimation of sugar content in wine grapes via in situ vnir–swir point spectroscopy using explainable artificial intelligence techniques. *Sensors*, 23(3).

[10] Lin, M., Chen, Q., and Yan, S. (2014). Network in network.

[11] Palumbo, M., Cefola, M., Pace, B., Attolico, G., and Colelli, G. (2023). Computer vision system based on conventional imaging for non-destructively evaluating quality attributes in fresh and packaged fruit and vegetables. *Postharvest Biology and Technology*, 200:112332.

[12] Polvara, R., Molina, S., Hroob, I., Papadimitriou, A., Tsiolis, K., Giakoumis, D., Likothanassis, S., Tzovaras, D., Cielniak, G., and Hanheide, M. (2024). Bacchus long-term (blt) data set: Acquisition of the agricultural multimodal blt data set with automated robot deployment. *Journal of Field Robotics*, 41(7):2280–2298.

[13] Ronneberger, O., Fischer, P., and Brox, T. (2015). U-net: Convolutional networks for biomedical image segmentation. In Navab, N., Hornegger, J., Wells, W. M., and Frangi, A. F., editors, *Medical Image Computing and Computer-Assisted Intervention – MICCAI 2015*, pages 234–241, Cham. Springer International Publishing.

[14] The Canopies Consortium (2021). Dimensioning of the real-world scenario for final demo. Available at <https://ec.europa.eu/research/participants/documents/downloadPublic?documentIds=>

080166e5e3eb6ac0&appId=PPGMS. Accessed: 03/29/2024.

[15] Tsakiridis, N. L., Samarinas, N., Kokkas, S., Kalopesa, E., Tziolas, N. V., and Zalidis, G. C. (2023). In situ grape ripeness estimation via hyperspectral imaging and deep autoencoders. *Computers and Electronics in Agriculture*, 212:108098.

[16] Underwood, J., Wendel, A., Schofield, B., McMurray, L., and Kimber, R. (2017). Efficient in-field plant phenomics for row-crops with an autonomous ground vehicle. *Journal of Field Robotics*, 34(6):1061–1083.

[17] Vrochidou, E., Bazinas, C., Manios, M., Papakostas, G. A., Pachidis, T. P., and Kaburlasos, V. G. (2021). Machine vision for ripeness estimation in viticulture automation. *Horticulturae*, 7(9).

[18] Williams, D., Britten, A., McCallum, S., Jones, H., Aitkenhead, M., Karley, A., Loades, K., Prashar, A., and Graham, J. (2017). A method for automatic segmentation and splitting of hyperspectral images of raspberry plants collected in field conditions. *Plant Methods*, 13(1):74.

[19] Williams, H., Harvey, S., McGuinness, B., Smith, D., Lim, H., and Duke, M. (2024). The barracuda: A novel cutting mechanism for pruning canes wrapped around wires. In *2024 IEEE 20th International Conference on Automation Science and Engineering (CASE)*, pages 3286–3293.

[20] Williams, H., Smith, D., Shahabi, J., Gee, T., Nejati, M., McGuinness, B., Black, K., Tobias, J., Jangali, R., Lim, H., Duke, M., Bachelor, O., McCulloch, J., Green, R., O’Connor, M., Gounder, S., Ndaka, A., Burch, K., Fourie, J., Hsiao, J., Werner, A., Agnew, R., Oliver, R., and MacDonald, B. A. (2023). Modelling wine grapevines for autonomous robotic cane pruning. *Biosystems Engineering*, 235:31–49.

[21] Xia, Z., Wu, D., Nie, P., and He, Y. (2016). Non-invasive measurement of soluble solid content and ph in kyoho grapes using a computer vision technique. *Anal. Methods*, 8:3242–3248.

[22] Xiong, Y., Ge, Y., Grimstad, L., and From, P. J. (2020). An autonomous strawberry-harvesting robot: Design, development, integration, and field evaluation. *Journal of Field Robotics*, 37(2):202–224.

[23] Xiong, Y., Peng, C., Grimstad, L., From, P. J., and Isler, V. (2019). Development and field evaluation of a strawberry harvesting robot with a cable-driven gripper. *Computers and Electronics in Agriculture*, 157:392–402.

[24] Zhou, B., Khosla, A., Lapedriza, A., Oliva, A., and Torralba, A. (2016). Learning deep features for discriminative localization. In *Proceedings of the IEEE Conference on Computer Vision and Pattern Recognition*, pages 2921–2929.

Appendix A. Detailed dataset description

Data collection was part of a larger effort within the Canopies project, exploring different sensors across seasons. The first data collection was done in September-October 2021, using a smartphone camera and a Reflex camera. The second data collection took place in September 2022, utilizing a smartphone camera and a Realsense d435i. Although the d435i is an RGB-D device, we used it as a standard camera for °Brix and color estimation.

Table A.5 summarizes the different types of data collected during the two seasons. The naming of the splits in the following tables follows a descriptive naming used during the development of the dataset and the code. For ease of reference, we renamed the splits with simpler tags ($T1$, $T2$, $T3$) to avoid bloated experiment descriptions. The match between the splits names given in Table 1 and A.7 are the following:

$T1_{STD} \rightarrow 2021PhoneJPG_reduced$
 $T1_{WB} \rightarrow 2021PhoneJPG_WB_reduced$
 $T2_{STD} \rightarrow Season21ToSeason22Phone$
 $T2_{WB} \rightarrow Season21ToSeason22Phone_WB$
 $T2_{ALL} \rightarrow Season21ToSeason22All$
 $T3_{STD} \rightarrow MixedSeason$
 $T3_{WB} \rightarrow MixedSeason_WB$

The data organization allows for testing covariate shifts due to both sensor type and season. These atomic splits represent minimal groups sharing the same sensor, season, image type, and label characteristics. Using these atomic splits, we designed the experimental splits, summarized in Table A.6 and Table A.7.

Images: Smartphone images were acquired at a resolution of 3000x4000 pixels, in both JPG and raw formats, with a few exceptions. Reflex images, captured in raw format, have a resolution of 3900x2613 pixels. The d435i RGB images have a lower resolution of 1280x720 pixels. Raw images were corrected for white balance using a gray card (Fig.2). Not all images included a gray card due to collection errors, but these images were still used for comparison purposes. The full images were labeled with bounding boxes around the grape bunches and then cropped. The resulting cropped images have very different sizes since some images were close-ups while others contained multiple targets. The combination of season, sensor used, gray card presence, and other factors creates differences summarized in Table A.5. The rows in the table represent *atomic splits*, i.e., splits with the same distribution. In contrast, between the splits, there is some form of covariate shift that we aim to study.

Appendix B. Hyper-parameters Exploration for the Histogram based Estimators

Following from Section 3.2, here we give the details of the hyper-parameter search for the histogram features.

Table B.9 summarizes the hyper-parameter ranges investigated by this experiment. Most of them have been introduced in Section 2.2. In addition to those, here we add the investigation of the effect of the input image resolution (low_res: 320×240 , med_res: 640×480 , high_res: 1280×720). For the *cross* parameter, to avoid hyper-parameter explosion, we designed three possible configurations (*none*, *thin*, *fat*), as described in Section 2.2.

To identify the most relevant hyper-parameters, taking into account the non-linear interactions between the different features, we opted to train a random forest (RF) algorithm on the hyper-parameter values themselves, to predict the validation error. Using this technique allows for reading the importance score of the RF as an indicator of the relevance of each hyper-parameter [5]. Figure B.11a shows the importance factors for the RF regressor trained to predict the validation error from the hyper-parameter values. The importance factor show which features contributes the most to the RF regression of the validation error, allowing for concluding that the *different starting image resolutions have little influence on the SSC estimation*. This is a relevant finding, since it allow us to safely work with the lowest resolution images without trading for estimation accuracy. Among the most important variables we find the ones that control the model flexibility, i.e. the regularization parameter, the x and y bin number, and the cross parameters, that impact the feature vector length. Together these parameters have to balance prediction power with the risk of over-fitting.

Finally, the color space show some relevance too. The correlation coefficient has already been shown in Fig. 8a, and its replicated in Fig. B.11b for convenience. Image resolution was omitted and the total histogram length (*feature_len*) was added. That histogram helps understanding which variable linearly correlates with the validation error, in positive or negative way, but alone it's not enough to show feature importance, since there could be some interactions effects between them.

To further explore this influence of feature flexibility due to histogram length, we show in Figure B.12 the correlation between the validation error and the most important hyper-parameters extracted from Figure B.11a, explicitly adding *feature_lenght* and its interactions with α and $\log(\alpha)$. It is evident that the feature length is the most important factor among the others, and that the interaction between feature length and α is more than relevant. The general behavior that we can extract from this analysis is that the more are the bins of the histogram, the higher should be the α value, and together these two parameters are sufficient to explain a great deal of the validation error variability.

Appendix C. Hyper-parameters Exploration for the Multi-task DNN

This appendix follow the same principles described in the previous one. Table C.10 gives a summary of the hyper-parameters ranges explored in the sweep. Given the huge parameter space, this time the sweep was performed with random sampling, with a total run count of 4912 (see Section 3.3). Figures C.13a and C.14a show importance values for the RF trained on the

| Dataset Id | Year | Smartphone | | | | Reflex | | d435i | | | Num images | Num samples | Expert GT | Color GT |
|------------|------|------------|-----|-----|------|--------|------|-------|-----|------|------------|-------------|-----------|----------|
| | | Type | Jpg | Raw | Card | Raw | Card | RGB | IR | Card | | | | |
| A | 2021 | motog8 | yes | no | no | no | - | no | no | - | 100 | 100 | no | no |
| B | 2021 | motog8 | no | yes | yes | yes | yes | no | no | - | 38 | 38 | possible | yes |
| C | 2021 | motog8 | yes | yes | yes | yes | yes | no | no | - | 62 | 62 | possible | yes |
| D | 2021 | motog8 | yes | yes | yes | yes | yes | no | no | - | 50 | 50 | possible | yes |
| E | 2022 | realmi | yes | yes | no | no | - | yes | no | no | 1 | 2 | no | no |
| F | 2022 | realmi | yes | yes | yes | no | - | yes | no | yes | 6 | 22 | possible | yes |
| G | 2022 | realmi | yes | yes | no | no | - | yes | no | yes | 1 | 2 | no | no |
| H | 2022 | realmi | yes | yes | yes | no | - | yes | no | yes | 4 | 19 | possible | yes |
| I | 2022 | motog8 | yes | yes | yes | no | - | yes | yes | yes | 8 | 51 | possible | yes |

Table A.5: Description of the atomic splits according to the device, image format, gray card presence, and the possibility of having expert ground truth from white-balanced images.

| Name | Components | Description |
|-------------------------|------------|--|
| 2021PhoneJPG | A+C+D | Contains all the jpg images collected with a smartphone in 2021, without white balance from the spits A, C, and D. |
| 2021PhoneJPG_reduced | C+D | Contains the jpg images collected with a smartphone in 2021 that have a corresponding white-balanced image. Corresponds to splits C and D. |
| 2021PhoneJPG_WB_reduced | C+D | Contain all the white-balanced images collected with a smartphone in 2021. Corresponds to splits C and D. |
| 2021PhoneJPG_WB | B+C+D | Contains all the jpg images collected with a smartphone in 2021, from splits B, C, and D |
| 2021ReflexJPG_WB | B+C+D | Contains all the jpg images collected with a reflex camera in 2021 from splits B, C, and D |
| 2022PhoneJPG_WB | F+H+I | Contains all the jpg images collected with a smartphone in 2022 from splits F, H, and I |
| 2022d435iAutoWB | F+H+I | Contains all the auto white balanced jpg images collected with d435i in 2022, from splits F, H, and I |

Table A.6: Description of the basic splits used to train and test the proposed algorithms.

| Name | Train set components | Test set components | Description |
|----------------------------|----------------------|---------------------|---|
| Season21ToSeason22Phone | A+C+D | F+H+I | All jpg images taken with a phone. |
| Season21ToSeason22Phone_WB | B+C+D | F+H+I | All raw images taken with a phone that have been white-balanced. |
| Season21ToSeason22All_WB | B+C+D | F+H+I | All phone and reflex images white-balanced. |
| Phone_d435i_Std | A+C+D+F+H+I | | All phone images not white-balanced, plus all d435i images |
| AllWB_d435i_Std | B+C+D+F+H+I | | All phone and reflex images white-balanced, plus all d435i images |
| MixedSeason_JPG | A+C+D+H+I | F | All jpg images, keeping for testing only the ones with the most uncertain brix value (around 16). |
| MixedSeason_WB_WB | B+C+D+H+I | F | All white balanced images, keeping for test only the most uncertain brix value (around 16). |

Table A.7: This table describes the most complex data splits, which we called *mixed splits*. These splits span across different sensors, while the train and test separation is based on the season.

hyper-parameter values to predict validation BCH respectively for $T2_{STD}$ (*Season21ToSeason22_Phone*) and $T3_{STD}$ (*Mixed-Season*). Finally, Tables 4, C.11, C.13, C.14, and C.12 summarize the best 10 runs respectively on $T2_{STD}$, $T2_{WB}$, $T3_{STD}$, $T3_{WB}$ and $T2_{ALL}$.

| Split name | #samples | $Brix_{mean}$ | $Brix_{std}$ | $Brix_{mae}$ | CC_1 | CC_2 | CC_3 | CC_4 | CC_5 | CC_6 |
|----------------------------------|----------|---------------|--------------|--------------|--------|--------|--------|--------|--------|--------|
| 2021PhoneJPG | 212 | 16.23 | 2.52 | 2.02 | 0.01 | 0.04 | 0.09 | 0.14 | 0.27 | 0.45 |
| 2021PhoneJPG_WB | 150 | 17.54 | 2.46 | 2.04 | 0.01 | 0.03 | 0.06 | 0.10 | 0.21 | 0.59 |
| 2021PhoneJPG_reduced | 112 | 17.19 | 2.43 | 1.99 | 0.01 | 0.04 | 0.07 | 0.12 | 0.22 | 0.54 |
| 2021PhoneJPG_WB_reduced | 112 | 17.19 | 2.43 | 1.99 | 0.01 | 0.04 | 0.07 | 0.12 | 0.22 | 0.54 |
| 2022PhoneJPG | 92 | 18.91 | 2.16 | 1.71 | 0.01 | 0.03 | 0.15 | 0.16 | 0.37 | 0.27 |
| 2022PhoneJPG_WB | 92 | 18.91 | 2.16 | 1.71 | 0.01 | 0.03 | 0.15 | 0.16 | 0.37 | 0.27 |
| 2021ReflexJPG_WB | 150 | 17.54 | 2.46 | 2.04 | 0.01 | 0.03 | 0.06 | 0.10 | 0.21 | 0.59 |
| 2022d435iAutoWB | 92 | 18.91 | 2.16 | 1.71 | 0.01 | 0.03 | 0.15 | 0.16 | 0.37 | 0.27 |
| MixedSeason_train | 352 | 17.67 | 2.75 | 2.33 | 0.01 | 0.04 | 0.12 | 0.16 | 0.32 | 0.34 |
| MixedSeason_test | 44 | 15.96 | 1.68 | 1.36 | 0.00 | 0.00 | 0.09 | 0.09 | 0.27 | 0.55 |
| MixedSeason_WB_train | 440 | 18.27 | 2.40 | 1.98 | 0.01 | 0.04 | 0.10 | 0.13 | 0.27 | 0.46 |
| MixedSeason_WB_test | 44 | 15.96 | 1.68 | 1.36 | 0.00 | 0.00 | 0.09 | 0.09 | 0.27 | 0.55 |
| Season21ToSeason22Phone_train | 212 | 16.23 | 2.52 | 2.02 | 0.01 | 0.04 | 0.09 | 0.14 | 0.27 | 0.45 |
| Season21ToSeason22Phone_test | 92 | 18.91 | 2.16 | 1.71 | 0.01 | 0.03 | 0.15 | 0.16 | 0.37 | 0.27 |
| Season21ToSeason22Phone_WB_train | 150 | 17.54 | 2.46 | 2.04 | 0.01 | 0.03 | 0.06 | 0.10 | 0.21 | 0.59 |
| Season21ToSeason22Phone_WB_test | 92 | 18.91 | 2.16 | 1.71 | 0.01 | 0.03 | 0.15 | 0.16 | 0.37 | 0.27 |
| Season21ToSeason22All_WB_train | 300 | 17.54 | 2.46 | 2.04 | 0.01 | 0.03 | 0.06 | 0.10 | 0.21 | 0.59 |
| Season21ToSeason22All_WB_test | 92 | 18.91 | 2.16 | 1.71 | 0.01 | 0.03 | 0.15 | 0.16 | 0.37 | 0.27 |
| All_Std | 396 | 17.48 | 2.71 | 2.30 | 0.01 | 0.04 | 0.12 | 0.15 | 0.32 | 0.37 |
| All_Std_WB | 484 | 18.06 | 2.44 | 2.03 | 0.01 | 0.03 | 0.10 | 0.12 | 0.27 | 0.47 |

Table A.8: Basic statistics for all the *atomic* and *mixed splits* described in Table A.7. For each split the following statistics are listed: number of samples, average °Brix, standard deviation of the °Brix, °Brix mean absolute error, and the percentage of each color class in the dataset. The color classes are unbalanced towards the unripe color classes, since the ripe bunches were harvested every few days.

| Hyper-parameter | Range | description |
|--------------------|---|--|
| n_{bin_x} | 4, 8, 16 | number of image columns bins. |
| n_{bin_y} | 8, 16, 32 | number of image rows bins. |
| <i>cross</i> | "none", "thin" or "fat" | How many bins to drop for background elimination. See Eq.1 for details. |
| <i>color_space</i> | "none", "hsv" or "Lab" | Use of CIE-La*b*, HSV or RGB color coordinates. |
| <i>dataset</i> | low_res, med_res, high_res, wb_low_res, wb_med_res, wb_high_res | Image resolution, corresponding to 320×240 , 640×480 and 1280×720 respectively, in color corrected and standard form. |
| α | 0.33, 1, 3, 9, 27, 81, 243, 729 | Ridge Regression regularization parameter. |

Table B.9: Hyper-parameters ranges for the histogram feature based models.

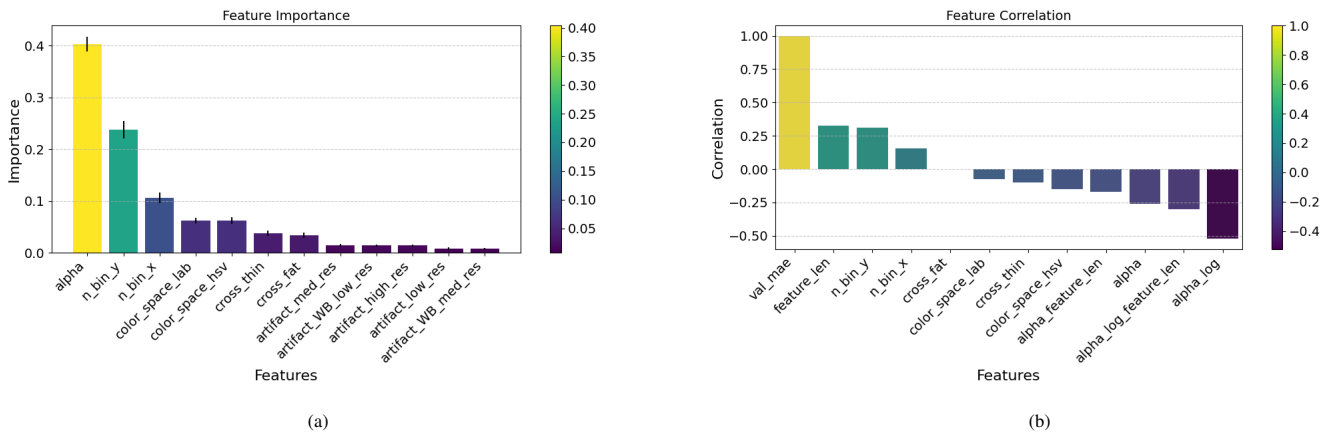


Figure B.11: a) Training a Random Forest using the hyper-parameters values to predict the validation error and then extracting the importance scores is a common way to extract the relative impact of each feature on the final estimator performance. Here we can see that the choice of initial image resolution is not relevant, while the regularization, the number of bins (that influence feature length and flexibility), and the color space have to carefully selected. b) shows the correlation computed on the 10% best performing runs. This plot complements the other, showing where the correlation with the error is positive or negative.

| Multi-task learning hyper-parameter | Range | description |
|---|--|--|
| α and β | 1, 10, 50, 100, 500, 1000 | The loss balancing factors (Eq. 2) |
| <i>batch_size</i> | 32, 64, 128 | Training batch size |
| <i>learning_rate</i> | 0.00001, 0.00005, 0.000001 | Initial learning rate, to be modified by the scheduling strategy |
| <i>learning_rate</i> | 0.00001, 0.00005, 0.000001 | Initial learning rate, to be modified by the scheduling strategy |
| <i>momentum</i> | 0.8, 0.9, 0.95, 0.99 | Momentum for the SGD optimizer |
| <i>im_height</i> and <i>im_width</i> | 64, 128, 256 | The image starting sizes before feature extraction by the auto-encoder. |
| <i>blur_σ_min</i> and <i>blur_σ_max</i> | [0.01, 0.1, 0.5] and [2.0, 4.0] | Together they define the range for the Gaussian blur augmentation that is always applied. |
| <i>color_space</i> | "none", "hsv" or "Lab" | Use of CIE-La*b*, HSV or RGB color coordinates. |
| <i>one_cycle</i> | True or False | Whether to use of not the one cycle scheduling strategy [] |
| <i>pretrained</i> | True or False | Whether the resnet18 backbone is pretrained on ImageNet [] or not. |
| <i>dataset_split</i> | <i>Season21ToSeason22Phone</i> , <i>Season21ToSeason22Phone_WB</i> , <i>Season21ToSeason22All_WB</i> , <i>MixedSeason</i> , <i>MixedSeason_WB</i> | Image resolution, corresponding to 320 × 240, 640 × 480 and 1280 × 720 respectively, in color corrected and standard form. |
| α | 0.33, 1, 3, 9, 27, 81, 243, 729 | Ridge Regression regularization parameter. |

Table C.10: This Table summarizes the hyper-parameters descriptions for the Multi-task experiments. A wide range of hyper-parameters was explored using random search for a total of more than 5000 experimental runs. In this case, the dataset splits used are not to be considered a proper hyper-parameter, but as a defining subset of the parameter sweep, since the distribution shifts between them are considerable. They are included in this table for ease of reference.

| Val BCH | Val SSC MAE | Val Acc | <i>alpha</i> | <i>beta</i> | <i>im_width</i> | <i>im_height</i> | <i>momentum</i> | <i>learning_rate</i> | <i>batch_size</i> | <i>blur_σ_min</i> | <i>blur_σ_max</i> | <i>pretrained</i> | <i>one_cycle</i> | <i>HSV</i> | <i>Lab</i> | <i>augment_extra</i> |
|----------|-------------|----------|--------------|-------------|-----------------|------------------|-----------------|----------------------|-------------------|-------------------|-------------------|-------------------|------------------|------------|------------|----------------------|
| 4.100699 | 1.835277 | 0.478261 | 500 | 50 | 128 | 256 | 0.800000 | 0.000050 | 64 | 0.500000 | 2 | True | True | True | False | True |
| 4.132786 | 1.913489 | 0.576087 | 100 | 1 | 256 | 64 | 0.990000 | 0.000050 | 64 | 0.010000 | 2 | True | True | False | False | True |
| 4.384027 | 1.570156 | 0.554348 | 1000 | 10 | 256 | 256 | 0.990000 | 0.000001 | 32 | 0.010000 | 2 | True | False | False | False | True |
| 4.397698 | 1.605315 | 0.434783 | 500 | 10 | 128 | 128 | 0.800000 | 0.000050 | 32 | 0.500000 | 2 | False | True | False | True | True |
| 4.499346 | 1.982949 | 0.576087 | 100 | 100 | 256 | 256 | 0.950000 | 0.000050 | 64 | 0.010000 | 4 | True | True | True | False | False |
| 4.522784 | 1.714363 | 0.500000 | 1000 | 100 | 256 | 128 | 0.990000 | 0.000010 | 64 | 0.100000 | 2 | True | False | True | True | False |
| 4.552584 | 1.768912 | 0.489130 | 500 | 10 | 128 | 128 | 0.900000 | 0.000050 | 64 | 0.500000 | 2 | True | True | False | True | False |
| 4.558001 | 1.644159 | 0.445652 | 1000 | 500 | 256 | 128 | 0.800000 | 0.000010 | 32 | 0.100000 | 4 | False | True | False | True | False |
| 4.583944 | 1.916520 | 0.521739 | 500 | 10 | 256 | 256 | 0.950000 | 0.000010 | 64 | 0.500000 | 4 | False | False | False | False | True |
| 4.596296 | 1.968404 | 0.597826 | 100 | 1 | 64 | 64 | 0.990000 | 0.000050 | 32 | 0.100000 | 4 | True | True | True | False | True |

Table C.11: The best ten runs on *Season2021ToSeason2022_WB* split. Compared to the ones given in Table 4, both the SSC MAE estimation error and Color estimation accuracy show worse performance.

| Val BCH | Val SSC MAE | Val Acc | <i>alpha</i> | <i>beta</i> | <i>im_width</i> | <i>im_height</i> | <i>momentum</i> | <i>learning_rate</i> | <i>batch_size</i> | <i>blur_σ_min</i> | <i>blur_σ_max</i> | <i>pretrained</i> | <i>one_cycle</i> | <i>HSV</i> | <i>Lab</i> | <i>augment_extra</i> |
|----------|-------------|----------|--------------|-------------|-----------------|------------------|-----------------|----------------------|-------------------|-------------------|-------------------|-------------------|------------------|------------|------------|----------------------|
| 3.977163 | 1.754222 | 0.576087 | 50 | 1 | 128 | 128 | 0.990000 | 0.000050 | 32 | 0.500000 | 2 | True | True | False | True | True |
| 4.123796 | 1.945782 | 0.532609 | 100 | 10 | 128 | 128 | 0.950000 | 0.000050 | 64 | 0.010000 | 2 | False | False | True | False | False |
| 4.269722 | 1.610763 | 0.673913 | 500 | 500 | 256 | 256 | 0.990000 | 0.000010 | 64 | 0.100000 | 4 | True | True | True | False | True |
| 4.307943 | 1.754948 | 0.608696 | 500 | 10 | 128 | 256 | 0.950000 | 0.000010 | 32 | 0.100000 | 2 | True | True | False | False | False |
| 4.327728 | 1.697267 | 0.467391 | 1000 | 50 | 128 | 128 | 0.950000 | 0.000010 | 32 | 0.500000 | 4 | False | True | False | True | False |
| 4.336076 | 1.930476 | 0.532609 | 1000 | 10 | 64 | 256 | 0.800000 | 0.000050 | 64 | 0.010000 | 2 | True | False | False | True | False |
| 4.347323 | 1.688515 | 0.500000 | 500 | 100 | 256 | 256 | 0.900000 | 0.000010 | 64 | 0.100000 | 4 | False | False | False | True | True |
| 4.411548 | 1.531855 | 0.597826 | 500 | 50 | 256 | 256 | 0.990000 | 0.000010 | 32 | 0.500000 | 2 | False | False | False | False | False |
| 4.440626 | 1.685545 | 0.630435 | 1000 | 500 | 256 | 256 | 0.990000 | 0.000001 | 128 | 0.100000 | 2 | False | False | True | False | False |
| 4.501309 | 1.803873 | 0.608696 | 1000 | 10 | 256 | 256 | 0.800000 | 0.000050 | 64 | 0.100000 | 4 | True | False | False | True | True |

Table C.12: The best ten runs on *Season2021ToSeason2022All_WB* split.

| Val BCH | Val SSC MAE | Val Acc | <i>alpha</i> | <i>beta</i> | <i>im_width</i> | <i>im_height</i> | <i>momentum</i> | <i>learning_rate</i> | <i>batch_size</i> | <i>blur_σ_min</i> | <i>blur_σ_max</i> | <i>pretrained</i> | <i>one_cycle</i> | <i>HSV</i> | <i>Lab</i> | <i>augment_extra</i> |
|----------|-------------|----------|--------------|-------------|-----------------|------------------|-----------------|----------------------|-------------------|-------------------|-------------------|-------------------|------------------|------------|------------|----------------------|
| 1.581554 | 1.200569 | 0.795455 | 500 | 10 | 128 | 64 | 0.900000 | 0.000050 | 32 | 0.010000 | 2 | True | False | True | False | True |
| 1.662561 | 1.116875 | 0.772727 | 1000 | 50 | 256 | 128 | 0.990000 | 0.000010 | 32 | 0.100000 | 4 | True | False | False | False | True |
| 1.686950 | 1.162343 | 0.772727 | 1000 | 50 | 256 | 256 | 0.950000 | 0.000010 | 32 | 0.010000 | 4 | True | True | False | True | False |
| 1.732328 | 1.231537 | 0.795455 | 50 | 100 | 256 | 256 | 0.950000 | 0.000010 | 32 | 0.010000 | 4 | False | False | True | False | True |
| 1.741897 | 1.102953 | 0.795455 | 1000 | 1000 | 64 | 64 | 0.990000 | 0.000001 | 32 | 0.500000 | 4 | False | True | False | True | True |
| 1.745264 | 1.301862 | 0.795455 | 1000 | 1000 | 128 | 128 | 0.950000 | 0.000001 | 32 | 0.100000 | 4 | False | True | False | False | False |
| 1.746910 | 1.269346 | 0.818182 | 1000 | 1000 | 256 | 256 | 0.900000 | 0.000010 | 128 | 0.100000 | 2 | True | True | False | True | False |
| 1.771968 | 1.174211 | 0.795455 | 100 | 500 | 64 | 128 | 0.950000 | 0.000010 | 64 | 0.100000 | 4 | False | False | False | False | True |
| 1.788137 | 1.190380 | 0.772727 | 100 | 50 | 128 | 256 | 0.950000 | 0.000050 | 128 | 0.500000 | 4 | False | False | False | False | False |
| 1.788171 | 1.242672 | 0.818182 | 10 | 10 | 256 | 256 | 0.950000 | 0.000050 | 64 | 0.100000 | 4 | True | True | False | False | True |

Table C.13: The best ten runs on *MixedSeason (T3_{STD})* split. The validation set is the same as for the *MixedSeason_WB (T3_{WB})*, that is collected with a d435i camera. Since the images from this device are automatically white balanced, this imply that the model faces a strong covariate shift due to different camera device and image modality.

| Val BCH | Val SSC MAE | Val Acc | <i>alpha</i> | <i>beta</i> | <i>im_width</i> | <i>im_height</i> | <i>momentum</i> | <i>learning_rate</i> | <i>batch_size</i> | <i>blur_σ_min</i> | <i>blur_σ_max</i> | <i>pretrained</i> | <i>one_cycle</i> | <i>HSV</i> | <i>Lab</i> | <i>augment_extra</i> |
|----------|-------------|----------|--------------|-------------|-----------------|------------------|-----------------|----------------------|-------------------|-------------------|-------------------|-------------------|------------------|------------|------------|----------------------|
| 1.545861 | 1.307749 | 0.818182 | 50 | 100 | 64 | 128 | 0.800000 | 0.000050 | 32 | 0.500000 | 4 | True | True | False | False | False |
| 1.596429 | 1.101236 | 0.795455 | 100 | 100 | 128 | 256 | 0.800000 | 0.000010 | 128 | 0.010000 | 2 | False | False | True | False | False |
| 1.611784 | 1.219757 | 0.772727 | 500 | 1000 | 128 | 128 | 0.800000 | 0.000010 | 32 | 0.010000 | 4 | False | False | True | False | False |
| 1.639119 | 1.065401 | 0.727273 | 50 | 10 | 128 | 256 | 0.950000 | 0.000050 | 64 | 0.500000 | 2 | False | True | False | False | True |
| 1.688067 | 1.220433 | 0.750000 | 500 | 500 | 128 | 128 | 0.950000 | 0.000010 | 32 | 0.500000 | 4 | True | False | True | False | False |
| 1.709684 | 1.295742 | 0.704545 | 10 | 10 | 256 | 256 | 0.990000 | 0.000010 | 32 | 0.010000 | 2 | True | False | False | True | False |
| 1.715017 | 1.159092 | 0.772727 | 100 | 100 | 64 | 128 | 0.800000 | 0.000050 | 32 | 0.100000 | 2 | True | False | True | False | False |
| 1.715871 | 1.158179 | 0.840909 | 10 | 10 | 256 | 256 | 0.900000 | 0.000050 | 64 | 0.100000 | 2 | True | False | True | False | True |
| 1.759702 | 1.200407 | 0.795455 | 50 | 50 | 128 | 128 | 0.900000 | 0.000050 | 128 | 0.100000 | 4 | False | False | True | False | False |
| 1.776299 | 1.200725 | 0.772727 | 100 | 50 | 256 | 256 | 0.900000 | 0.000050 | 32 | 0.010000 | 4 | True | True | True | False | False |

Table C.14: The best ten runs on *MixedSeason_WB (T3_{WB})* split. This time the results are comparable with the STD ones presented in Table C.13. This can be explained considering the fact that the validation images of the d435i are white-balanced and therefore with a similar hue to the color-corrected training images.

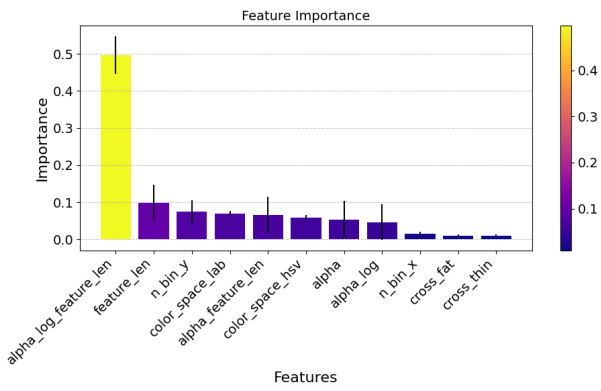
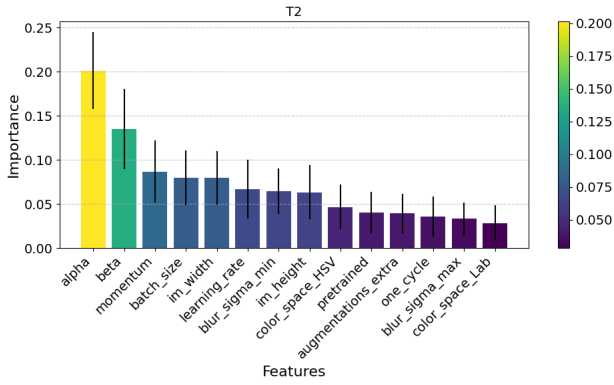
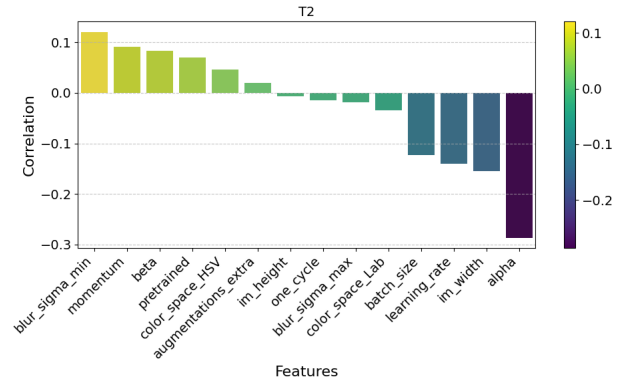


Figure B.12: To better extract the impact of feature length on validation error, we add three parameters to the analysis, $feature_len$ and its interactions with $alpha$ and $\log alpha$. It is easy to see that the length of the histogram is the most important hyper-parameter to be tuned for final model performance.

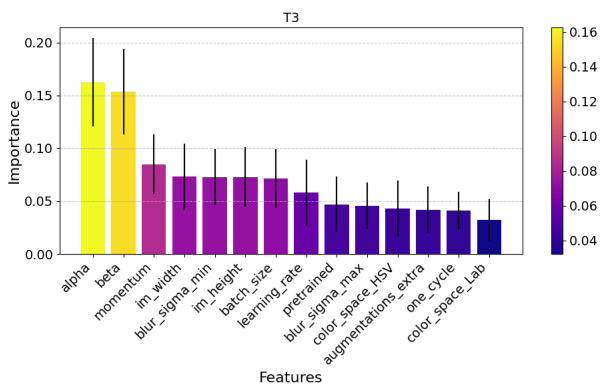


(a)

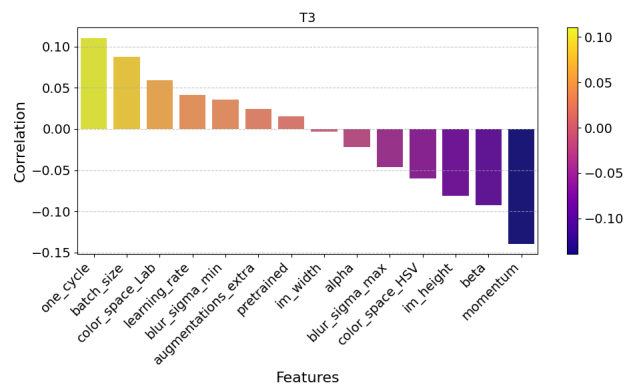


(b)

Figure C.13: a) These plots show the importance and correlation factor of the best 25% of the runs trained on the *Season2021ToSeason2022* dataset split. It can be noted that the main influence comes from the classical parameters that impact any DNN training (learning rate, batch size, regularization parameters), while the choice of image size and color space comes seems to be still relevant for the final performances. More insights on this can be extracted from Table 4.



(a)



(b)

Figure C.14: These plots show the importance and correlation factor of the best 25% of the runs trained on the *MixedSeason* dataset split.